



Supporting Information

for *Small*, DOI: 10.1002/smll.201800826

Mass Measurements Reveal Preferential Sorption of Mixed Solvent Components in Porous Nanoparticles

Mario M. Modena, Patrick Hirschle, Stefan Wuttke, and Thomas P. Burg**

Supporting Information

Mass Measurements Reveal Preferential Sorption of Mixed Solvent Components in Porous Nanoparticles

Mario M. Modena, Patrick Hirschle, Stefan Wuttke and Thomas P. Burg**

Dr. M. M. Modena

Max Planck Institute for Biophysical Chemistry, Am Faßberg 11, 37077 Göttingen, Germany

P. Hirschle

Department of Chemistry and Center for NanoScience (CeNS), University of Munich (LMU),
Butenandtstraße 11, 81377 Munich, Germany

Dr. S. Wuttke

Department of Chemistry and Center for NanoScience (CeNS), University of Munich (LMU),
Butenandtstraße 11, 81377 Munich, Germany

and

School of Chemistry, University of Lincoln, Joseph Banks Laboratories, Brayford Pool, Lincoln
LN6 7DL, United Kingdom

Email: stefan.wuttke@cup.uni-muenchen.de

Dr. T. P. Burg

Max Planck Institute for Biophysical Chemistry, Am Faßberg 11, 37077 Göttingen, Germany

Email: tburg@mpibpc.mpg.de

Table of Contents

Density measurements	3
Detection method	3
Experimental procedure	3
Method validation.....	4
Methods and Characterization of MIL-101(Cr) Nanoparticles.....	4
Synthesis of the Nanoparticle Samples	5
Synthesis of MIL-101(Cr) nanoparticles	5
Postsynthetic functionalization with pyridine and pyrazine.....	6
Characterization of the Nanoparticle species	6
X-ray Diffraction	6
Transmission Electron microscopy	7
Scanning Electron microscopy	11
Dynamic Light Scattering and Zeta-Potential measurements	20
Thermogravimetric Analysis	21
Elemental Analysis	22
Nitrogen Sorption	23
Porosity Estimation and Calculation of the density of dry MIL-101(Cr).....	24

Density measurements

Detection method

Figure S1 shows a schematic of the experimental setup and of the subsequent data analysis. The buoyant mass of the particles is measured in mixtures of two solvents with different densities and mixed at different concentrations, therefore obtaining solutions of different densities. The test solutions are prepared with equal particle concentration to avoid variations during the measurement and simplify the data analysis. The sample is then drawn into the SMR device by means of syringe pumps, while the flow velocity in the detection channel is controlled by pressurizing the chip inlets. The combination of pressure control and syringe pumps enables smooth pulse-free flow during measurement and precise estimation of the mixture composition throughout the measurement. The density of the solution at any time is estimated by measuring the frequency shifts induced by added reference particles of known volume and density, and by pre-calibration of the mass/frequency responsivity of the SMR.

After high-pass filtering of the time-domain mass trace and the removal of the reference particle signatures, the frequency fluctuations can be analyzed by means of the autocorrelation function. As white noise is largely confined to $\tau \leq 1/F_s$ in the autocorrelation function, where F_s is the sampling frequency, the estimation of $C(0)$ is obtained by fitting of the autocorrelation curve using an approximated fit function of the curve^[22]. Finally, the magnitudes of the autocorrelation curves are plotted against as functions of the density of the solutions and fitted with a parabola with zero minimum to estimate the intercept of the curve with the x-axis, which corresponds to the effective density of the particles in solution. Although only two measurements at different densities would be needed to fit the parabola, the resulting fit curve would present an ambiguity on the position of the curve minimum. The measurement scheme presented here enables the rapid acquisition of measurements at several solution densities, increasing the accuracy and reliability of the density estimation, and returning a unique solution of the fit parabola.

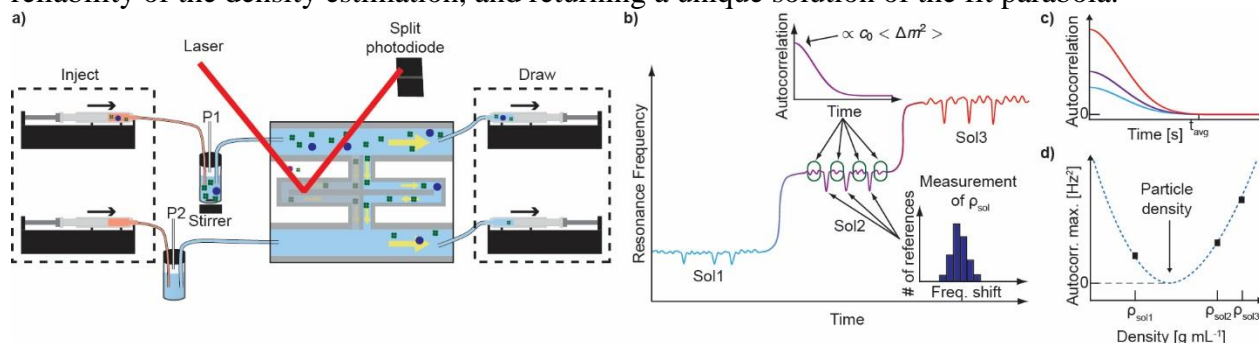


Figure S1 Measurement of particle density with SMRs. a) Schematic of the experimental setup, which includes (from the left): two syringe pumps for varying the solution density, pressurized inlets (P1 and P2) to control the flow in the microfluidic chip, an optical lever composed of a laser beam focused on the resonator and a split photodiode, two syringe pumps for drawing out the solution and precisely controlling the volume of solution flown in the chip; b) time-domain mass signal. The insets show the autocorrelation of small fluctuations of resonance frequency caused by the random number fluctuations of the nanoparticles in the channel (top) and the frequency shifts of the large calibration particles used for the detection of the solution density (bottom); c) the amplitude of the autocorrelation of the time-domain mass signal depends on the difference in density between the nanoparticles and the suspending solution; d) the amplitude of the autocorrelation as a function of solution density. The minimum of the fit parabola corresponds to the effective density of the particles in solution.

Experimental procedure

The SMR presents two large bypass channels for the rapid exchange of the solutions, and a torsional resonating structure with embedded microfluidic channels of $3 \times 8 \mu\text{m}^2$ cross-section (Height x Width). First, the sample and wash solutions are drawn into the SMR. Then, the direction and velocity of the flow inside the embedded microfluidic channel are controlled by pressurizing the vials containing the solutions. The density of the solutions is varied during the measurement by mixing them with known volumes of solutions with different density at specific times. Preparing the sample and the diluting solution with the same concentration of particles ensures constant sample concentration throughout the measurement.

The resonance frequency of the resonator is detected by using an optical lever readout scheme. The average resonance frequency varies with the density of the solution flowing in the embedded microfluidic channels. Particles of known size and density are added to the solution to estimate the density of the fluid at any moment from their induced transient shifts in resonance frequency.

Method validation

Characterization of polystyrene nanoparticles. As validation of the density characterization method, we measured the density of 210 nm (nominal size) polystyrene nanoparticles suspended in mixtures of pure water and ethanol by gradually increasing the ethanol fraction to 50% v/v. The variation of the autocorrelation amplitude with solution density is shown in Figure 2. The autocorrelation amplitude strongly increases with the ethanol concentration, clearly indicating that the particles have a density higher than that of pure water. Fitting of the experimental points with a parabola finds an effective mass density for the polystyrene nanoparticles of $\rho_{eff}^{EtOH/Water} = 1.056 \pm 0.001 \frac{\text{g}}{\text{cm}^3}$, which agrees with the manufacturer specifications^[28]. As expected, the polystyrene particles behave as hard spheres, which are impermeable to the solvent. From the known total solid content and the measurement of $\rho_{eff}^{EtOH/Water}$, we can calculate the mean mass $M_f = 4.03 \pm 0.36 \text{ fg}$ and the mean diameter $d_p = 194 \pm 6 \text{ nm}$ of the nanoparticles.

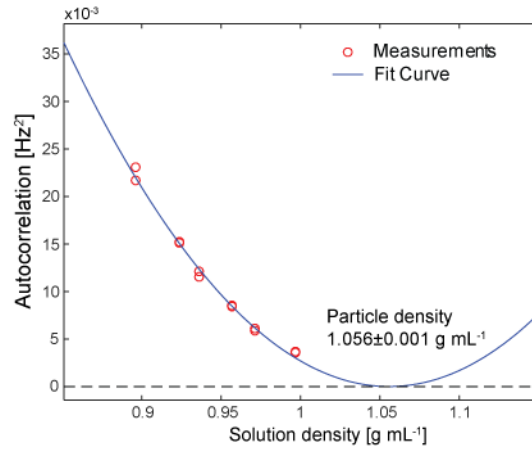


Figure S2. Density characterization of 210 nm (nominal size) polystyrene beads in mixtures of ethanol and water.

Methods and Characterization of MIL-101(Cr) Nanoparticles

Dynamic Light Scattering and Zeta-Potential. Dynamic light scattering experiments and measurements of Zeta-Potential were conducted with a *Zetasizer Nano Series* (Nano-ZS,

Malvern) featuring a laser with the wavelength $\lambda = 633$ nm. All DLS measurements were performed on the freshly synthesized samples in ethanol. Zeta-Potential measurements were performed in aqueous solution of the nanoparticles ($c = 0.1$ mg ml⁻¹). During the measurement, the pH was adjusted from pH = 2 to pH = 9 with a *MPT-2 Multi Purpose Titrator (Malvern)* using aqueous hydrochloric acid and sodium hydroxide solutions.

Scanning Electron Microscopy (SEM). The three MOF samples were examined on a *Helios NanoLab G3UC (FEI)* operating with 3 keV. The three samples were dried from ethanolic dispersions of the respective MOF species. Prior to the SEM measurements, the dried samples were additionally sputtered with carbon. The resulting micrographs from the SEM measurements were evaluated manually using the software *ImageJ v1.49*.

Transmission Electron Microscopy(TEM). All three MOF samples were examined using a *Titan Themis (FEI)* operated with an acceleration voltage of 300 kV. Sample preparation was performed via drying an ethanolic nanoparticle dispersion on a carbon-coated copper grid.

Thermogravimetry (TG). Dried samples of MIL-101(Cr) (5.90 mg), pyridine functionalized MIL-101(Cr) (6.20mg) and pyrazine functionalized MIL-101(Cr) (2.68mg) were examined on a *TASC 414/4 (Netzsch)* under synthetic air. The results of the experiments, which were performed employing a heating rate of 10 °C/min up to 900 °C, were evaluated with the included software *Proteus v4.3*.

Powder X-Ray Diffraction (PXRD). In order to confirm a successful synthesis of MIL-101(Cr) MOF and to check the intactness of the crystal structure after functionalization, X-ray diffraction was performed. The instrument used was a *STOE STADI P* system. The experiments were performed in a transmission configuration derived from the Debye-Scherrer geometry. All experiments were performed with CuK_{α1}-radiation. For data analysis the included software package *WinXPOW RawDat v3.0.2.5* and *WinXPOW PowDat_n v3.0.2.7* was used. The simulation of unfunctionalized MIL-101(Cr) bulk material was based on the structural data from the group of Férey¹ using the software *Materials Studio v7.0 (BIOVIA)*.

Nitrogen sorption. Ethanolic dispersions of the respective samples were dried in an oven at 70 °C for 3 days. The dried powders of each of the samples were outgassed in high vacuum (see Table S1). Nitrogen sorption experiments were performed with an *Autosorb-1 (Quantachrome)*. The results were evaluated using the software *ASiQwin v3.0*. The linearized form of the BET equation was used to calculate BET surface areas. For the calculation of the pore size distribution a QSDFT adsorption based model was used assuming slit, cylindrical, and spherical pores.

Table S1: Conditions employed during the outgassing of the samples.

MIL-101(Cr)	Pyridine-Functionalization	Pyrazine-Functionalization
38 h, 120 °C	72 h, 120 °C	38h, 70 °C

Synthesis of the Nanoparticle Samples

Synthesis of MIL-101(Cr) nanoparticles

The synthesis of MIL-101(Cr) was conducted using microwave (MW) assisted synthesis^[27]. A mixture of Cr(NO₃)₃ · 9 H₂O (1.48 g, 3.70 mmol) and terephthalic acid (0.615 g, 3.70 mmol) was added to water (20 ml, Milli-Q) and stirred until all Cu(NO₃)₃ · 9 H₂O was dissolved. Subsequently, the reaction mixture was placed in a Teflon tube (80 ml) and sealed. The tube was

placed in a microwave oven (*Synthos 3000, Anton-Paar*) along with 3 other vessels, two of them being filled with water (20ml) and one of them being a control vessel filled with an aqueous $\text{Cu}(\text{NO}_3)_3 \cdot 9 \text{H}_2\text{O}$ (1.48 g, 3.70 mmol) solution. The heating sequence shown in Table S2: MW Heating program for the MIL-101(Cr) synthesis Table S2 was applied:

Table S2: MW Heating program for the MIL-101(Cr) synthesis.

Heating	Dwelling	Cooling
4 min	2 min	1.5 h
To 210 °C	210 °C	To RT

The resulting nanoparticles were washed via centrifuging (20500 rpm, 45 min), removal of supernatant, and redispersing them under sonication in ethanol (30 ml). Subsequently the MOF nanoparticle dispersion was filtered in order to remove excess terephthalic acid. Afterwards, the nanoparticles were centrifuged (20500 rpm, 45 min), followed by removal of the supernatant and redispersing of the pellet under sonication for 3 additional times.

Postsynthetic functionalization with pyridine and pyrazine

For the pyrazine functionalization an ethanolic MIL-101(Cr) nanoparticle dispersion (7.2 ml, $c = 12.4 \text{ mg ml}^{-1}$) was added to an ethanolic pyrazine solution (7.2 ml, $c = 320 \text{ mg/ml}$, 4mM). The reaction mixture was kept stirring for 24 h. The resulting modified nanoparticles were washed in 4 cycles consisting of centrifuging (14000 rpm, 30 min), removal of supernatant and redispersing in ethanol under sonication.

For the pyridine functionalization, pyridine (12.2 ml, 154 mmol) was added to an ethanolic MIL-101(Cr) nanoparticle dispersion (7.2 ml, $c = 12.4 \text{ mg ml}^{-1}$) in addition to ethanol (2.2 ml). The reaction mixture was kept stirring for 24 h. The resulting modified nanoparticles were washed in 4 cycles consisting of centrifuging (14000 rpm, 30 min), removal of supernatant and redispersing in ethanol under sonication.

Characterization of the Nanoparticle species

X-ray Diffraction

The results of the X-ray diffraction experiments are shown in Figure S3. The PXRD data of all three MIL-101(Cr) species is in agreement with literature results^[29]. The reflex broadening in the MIL-101(Cr) nanoparticle samples is not caused by lack of crystallinity but by the nanosized crystalline domains, as can be seen in the TEM results.^[27]

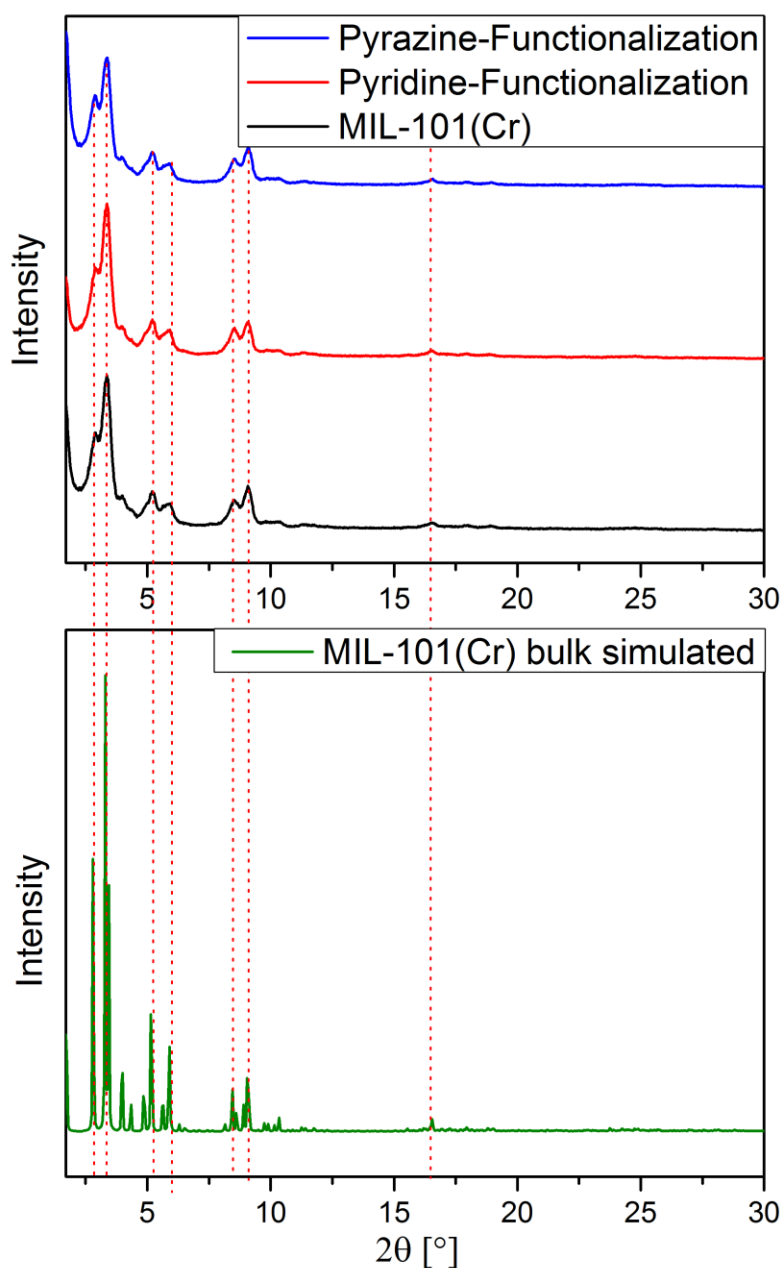


Figure S3: Powder X-ray diffraction patterns of the initial MIL-101(Cr) sample as well as the functionalized species.

Transmission Electron microscopy

Overview images gained from TEM measurements are shown in Figure S4, Figure S5, Figure S6 and for the respective samples. Generally, the micrographs prove the crystallinity of the MOF samples prior to and after functionalization with pyridine/pyrazine. For better comparison, detailed images for each of the respective species are shown in Figure S7.

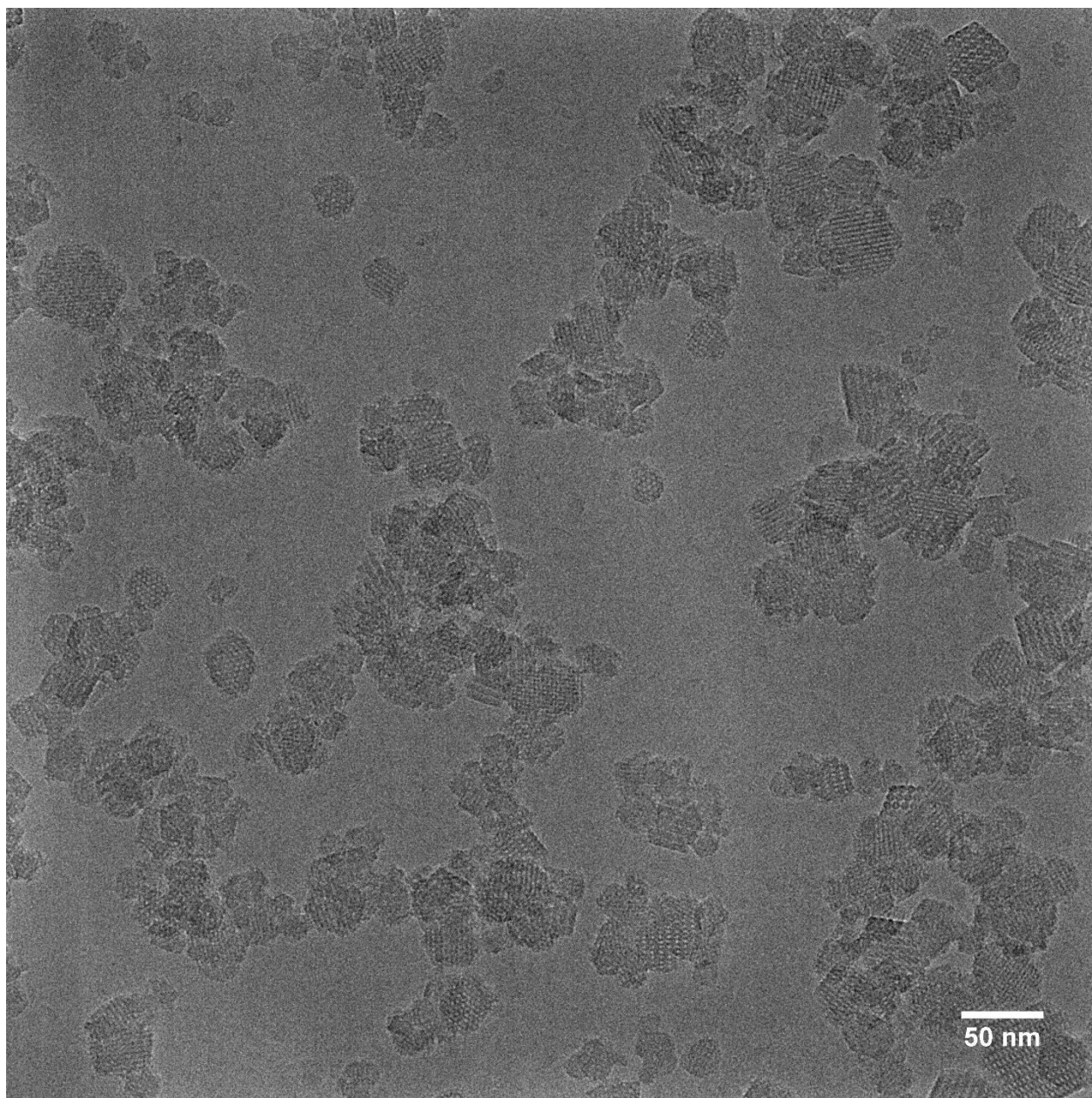


Figure S4: TEM micrograph of MIL-101(Cr).

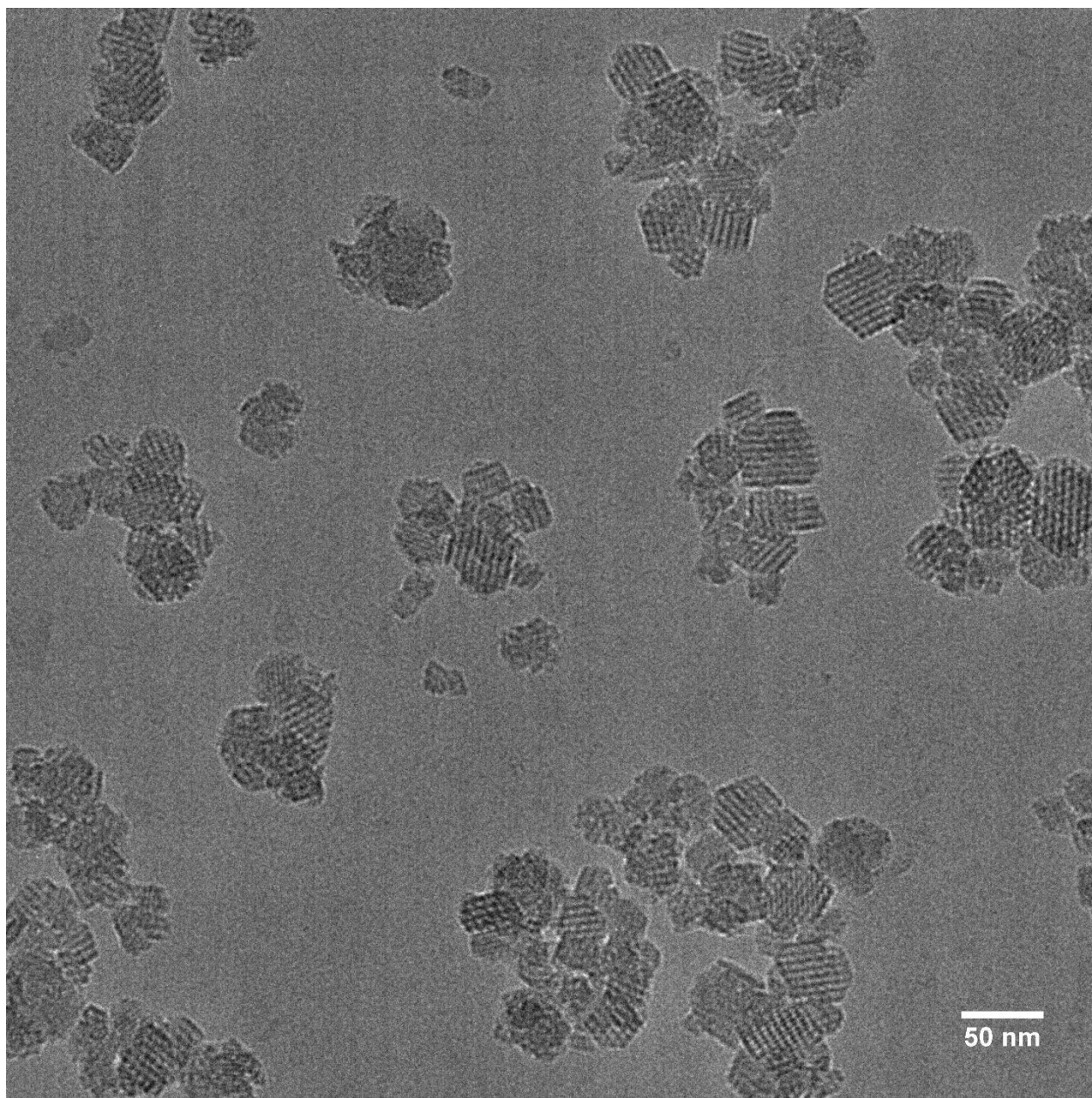


Figure S5: TEM micrograph of pyridine-functionalized MIL-101(Cr).

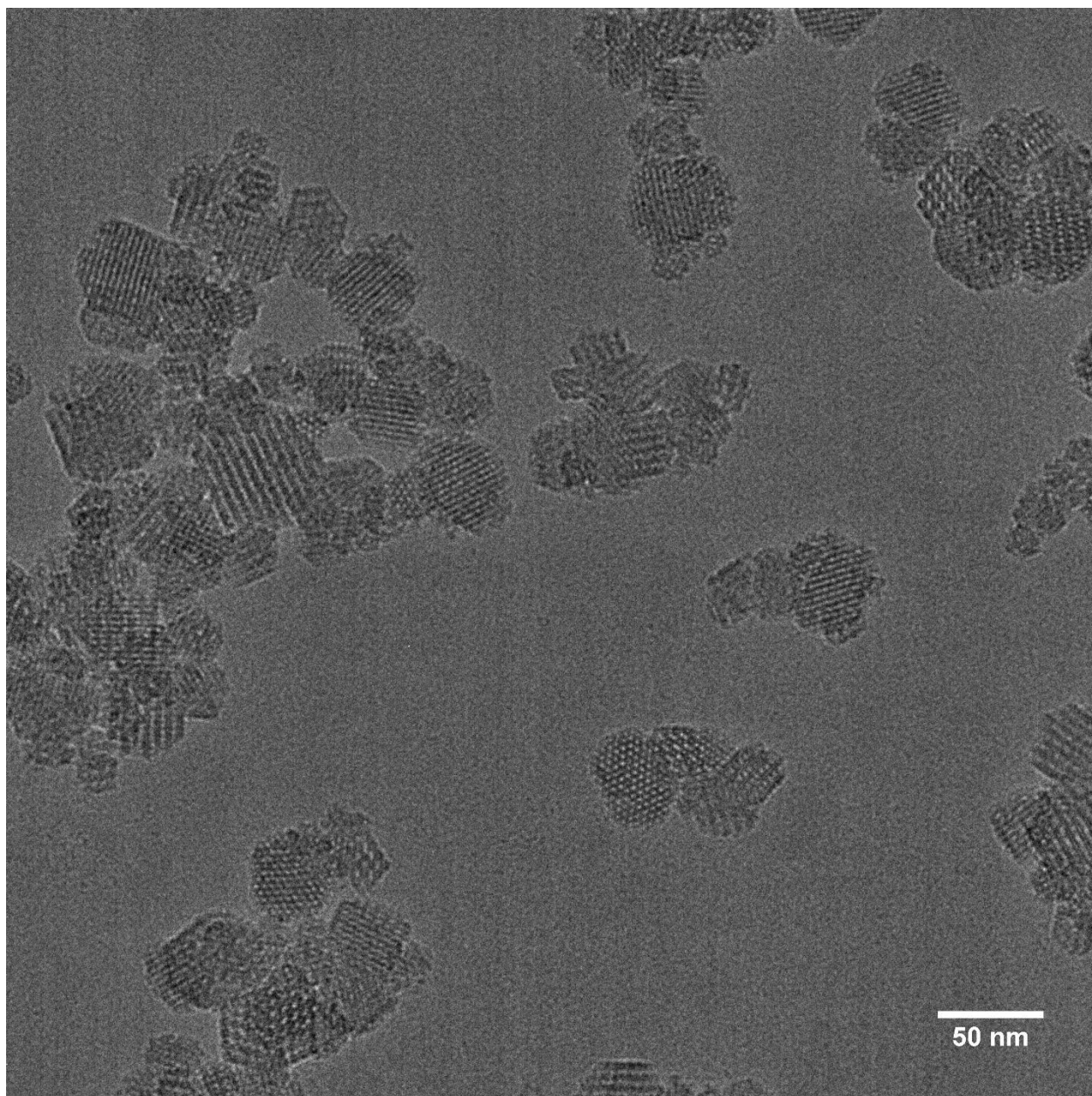


Figure S6: TEM micrograph of pyrazine-functionalized MIL-101(Cr).

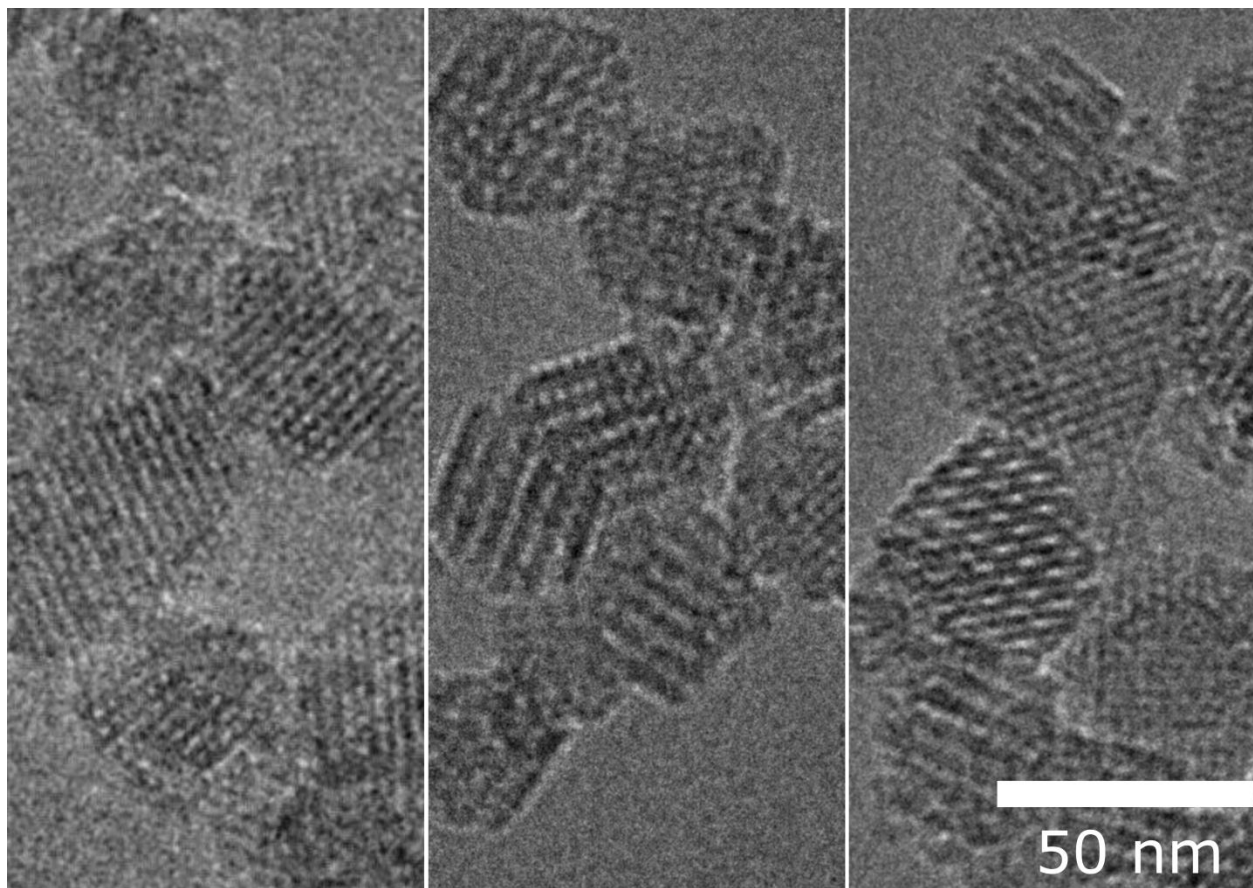


Figure S7: Zoomed-in micrographs of MIL-101(Cr) (left) and its pyridine-functionalized (middle) and pyrazine-functionalized (right) derivatives.

Scanning Electron microscopy

Figure S8, Figure S10 and S12 give an overview of the initial MIL-101(Cr) sample and the pyridine and pyrazine functionalized derivatives. Additionally in the top right corner of each of the micrographs, the nanoparticles, which have been used for particle size determination, are marked with yellow lines. All three samples look homogeneous. A more detailed view on the particles is shown in Figure S9, Figure S11 and Figure S13. Again, the samples look very similarly. The resulting particle size distributions for the dried species have been determined manually by measuring the diameter of ~100 particles of the respective species and are shown in Figure S14, Figure S15 and Figure S16, and are additionally summarized in Table S3.

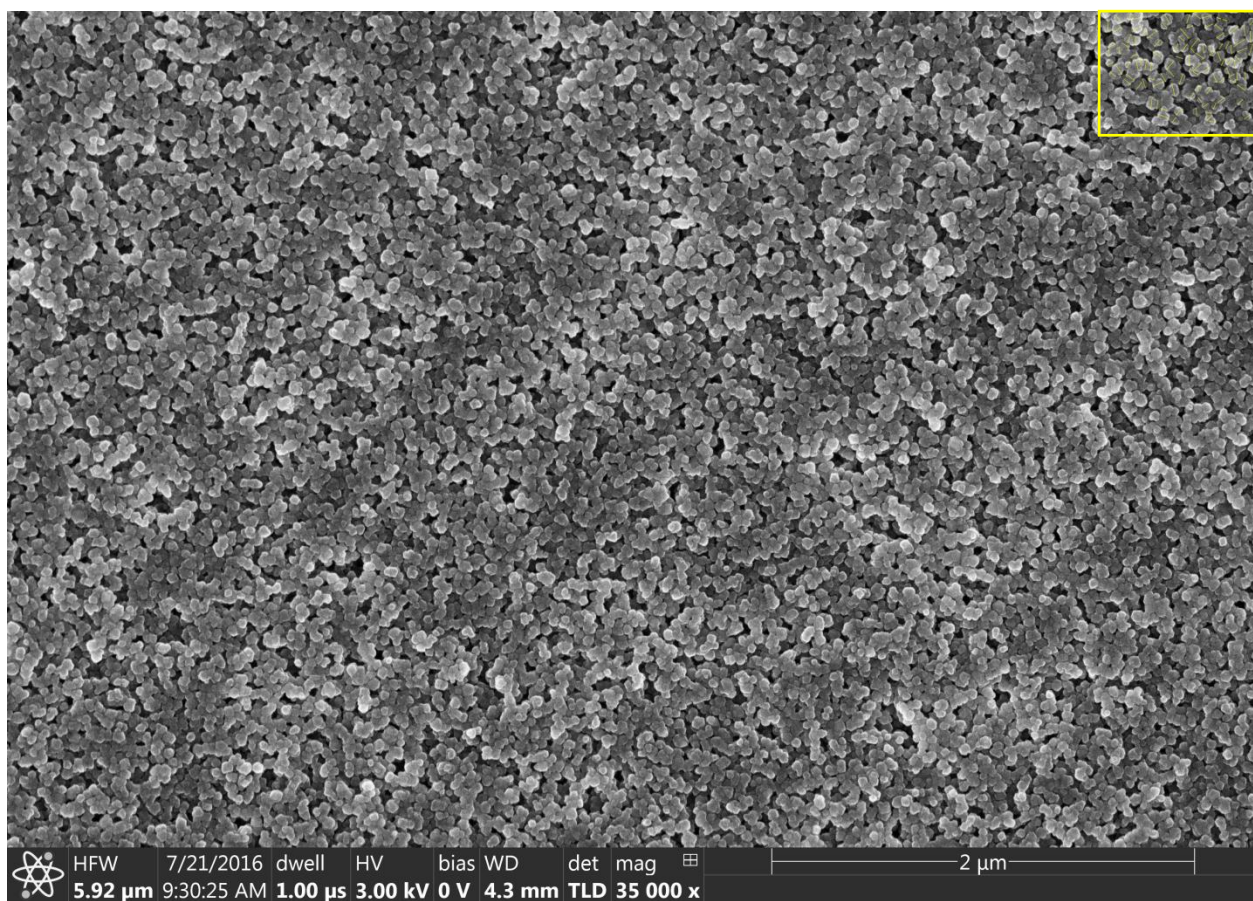


Figure S8: SEM micrograph of MIL-101(Cr). The particles that have been measured for size determination are marked by a yellow box in the top right corner.

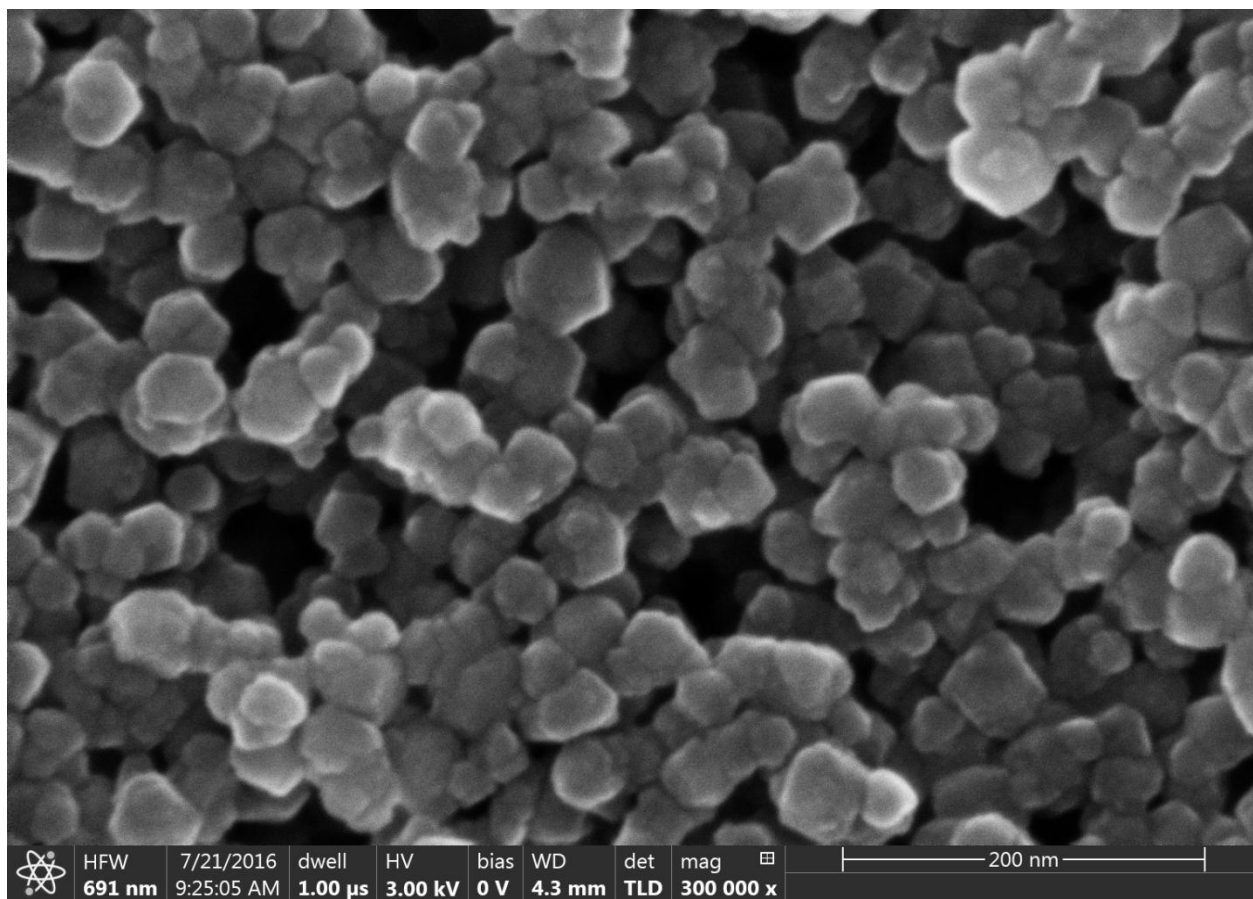


Figure S9: Additional close-up SEM micrograph of MIL-101(Cr) featuring a higher magnification.

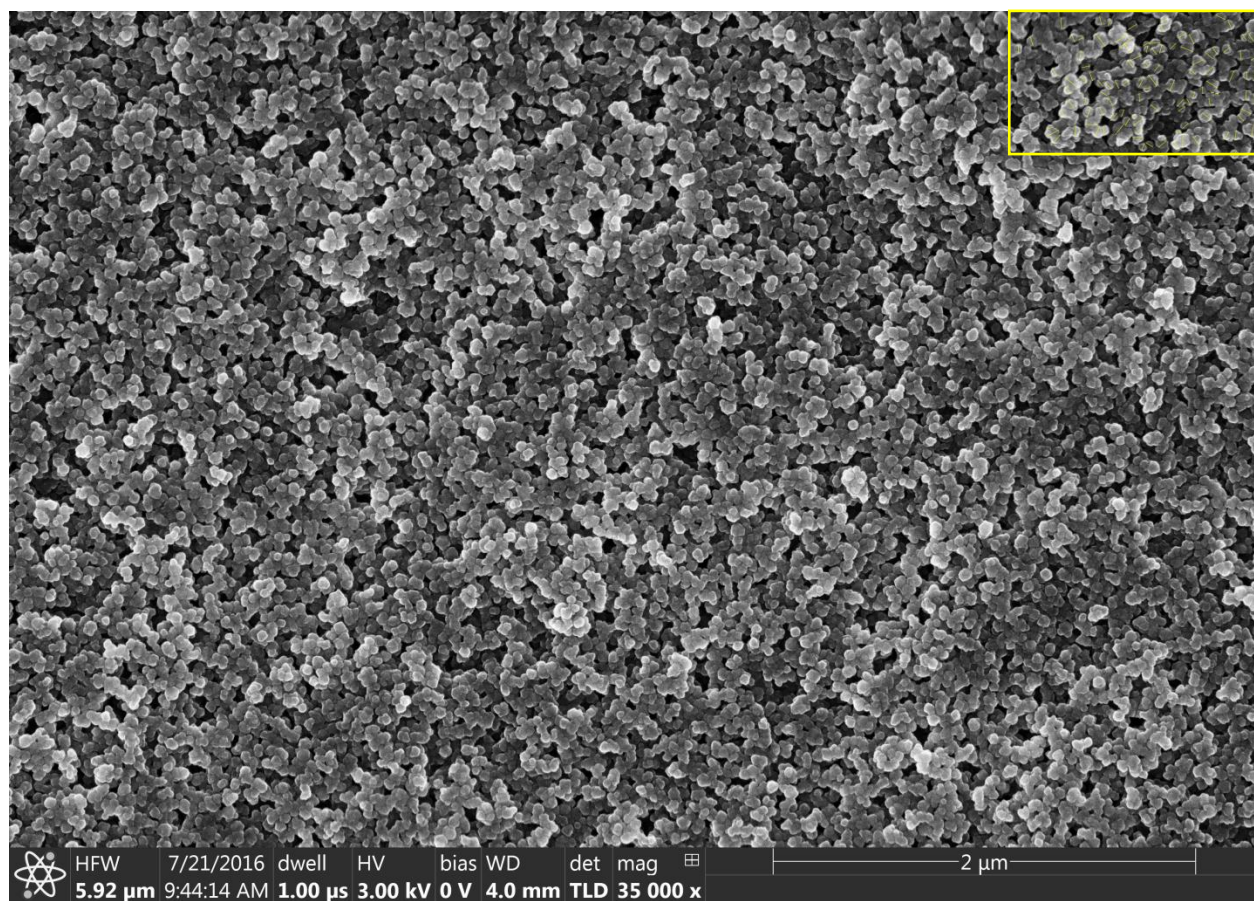


Figure S10: SEM micrograph of pyridine-functionalized MIL-101(Cr). The particles that have been measured for size determination are marked by a yellow box in the top right corner.

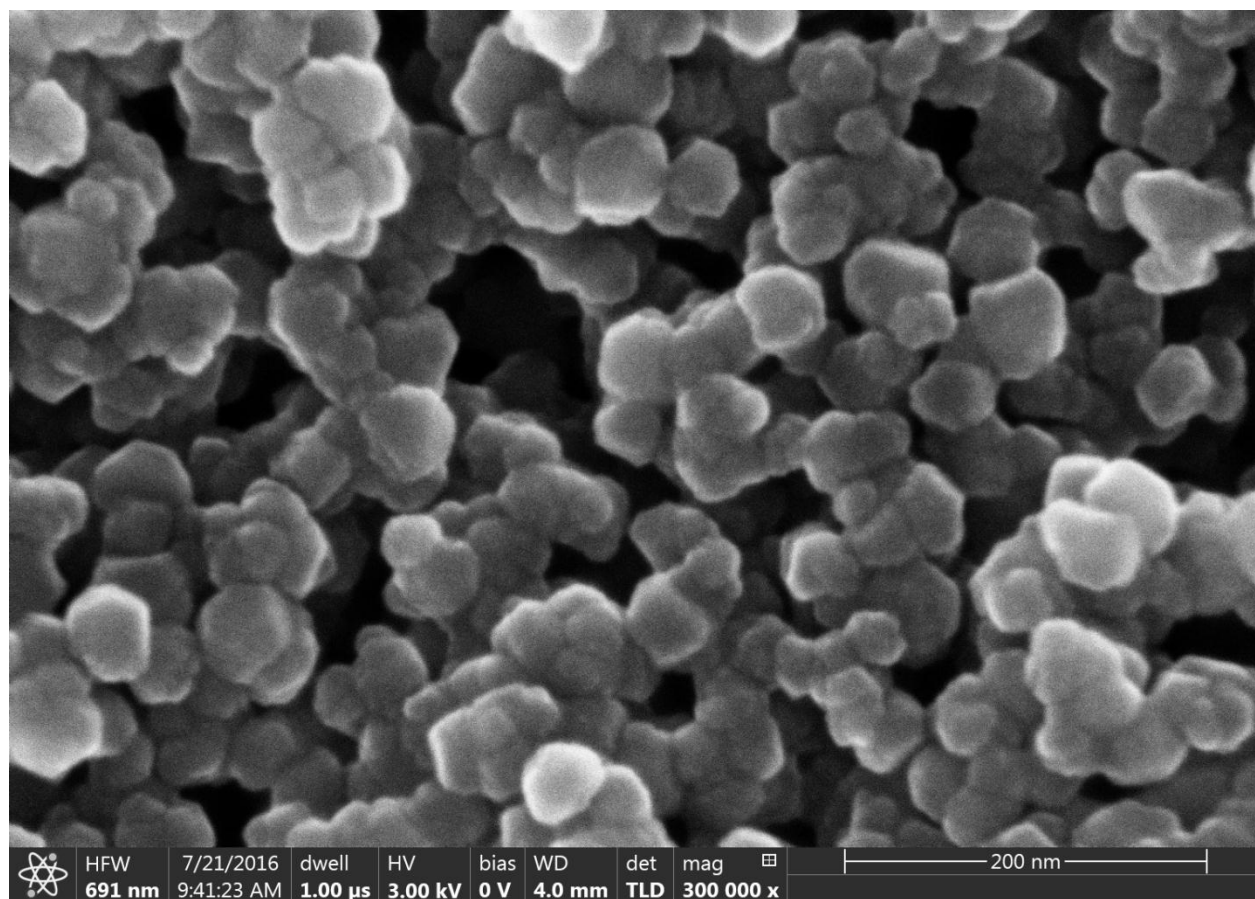


Figure S11: Additional close-up SEM micrograph of pyridine-functionalized MIL-101(Cr) featuring a higher magnification.

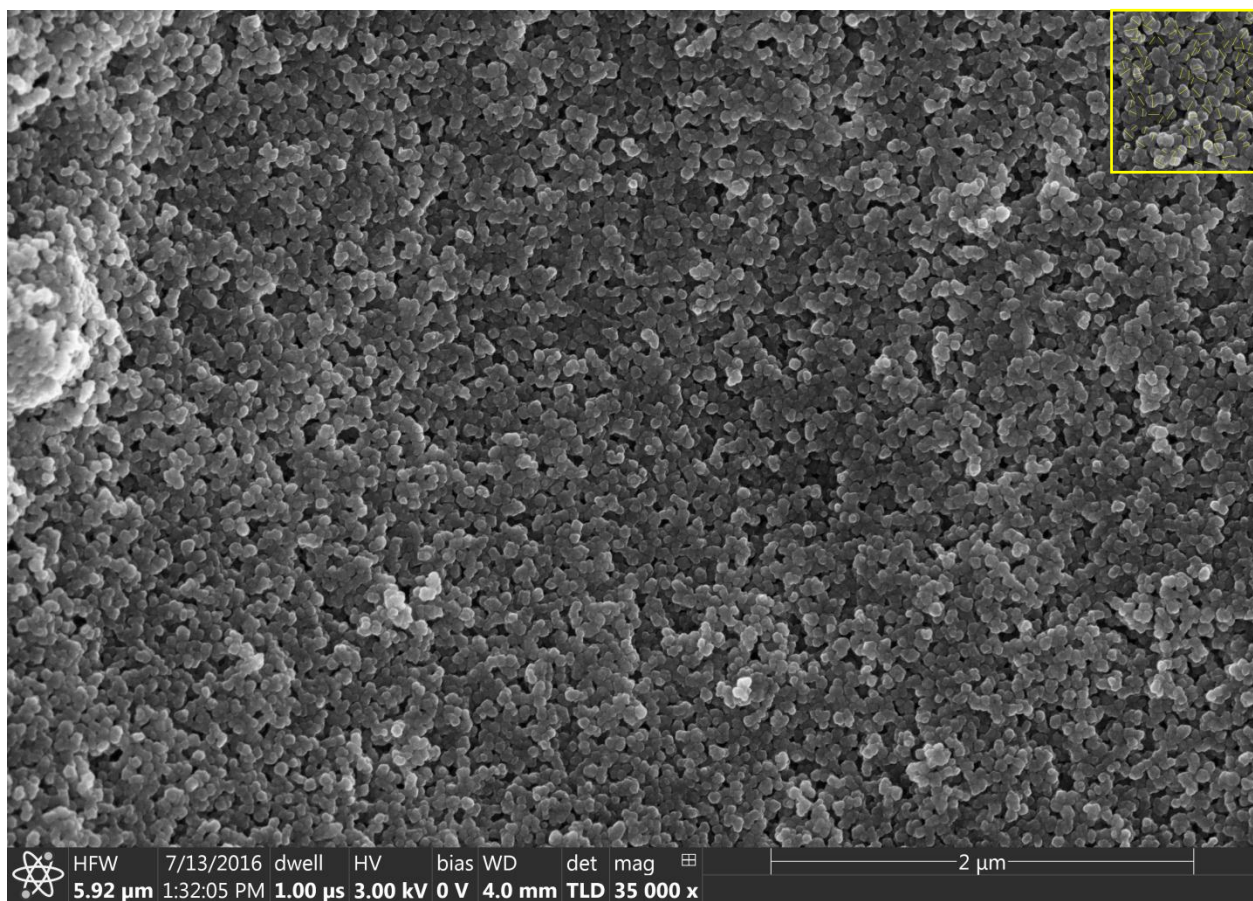


Figure S12: SEM Micrograph of pyrazine-functionalized MIL-101(Cr). The particles that have been measured for size determination are marked by a yellow box in the top right corner.

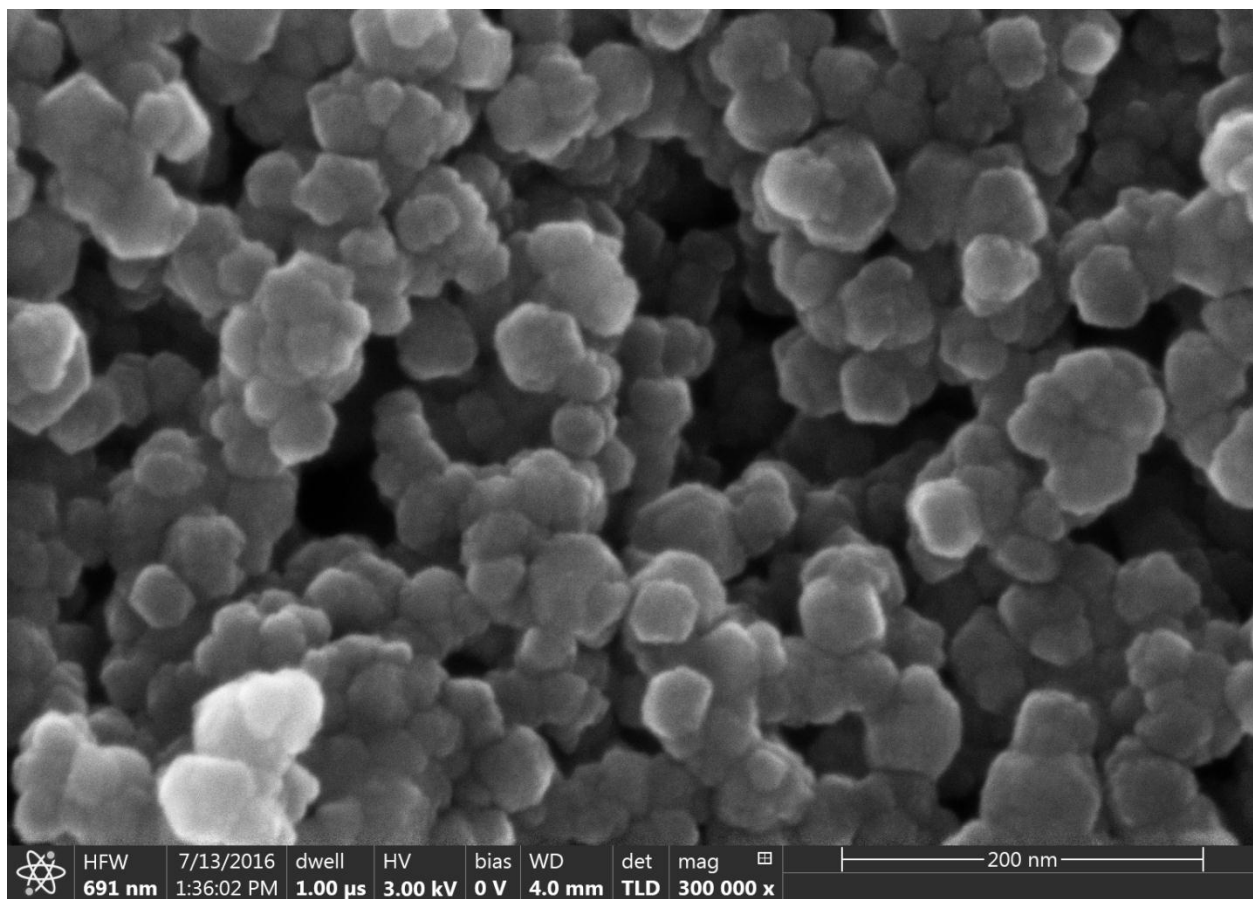


Figure S13 : Additional close-up SEM micrograph of pyrazine-functionalized MIL-101(Cr) featuring a higher magnification.

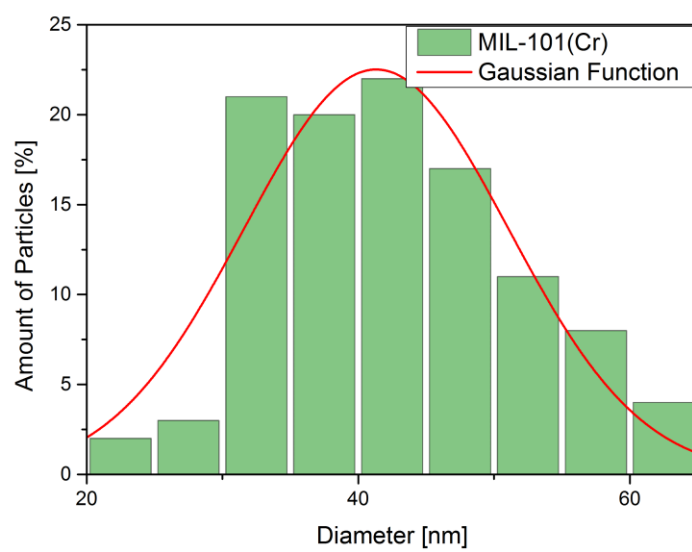


Figure S14: Particle size distribution of MIL-101(Cr) determined from the SEM micrograph in Figure S8.

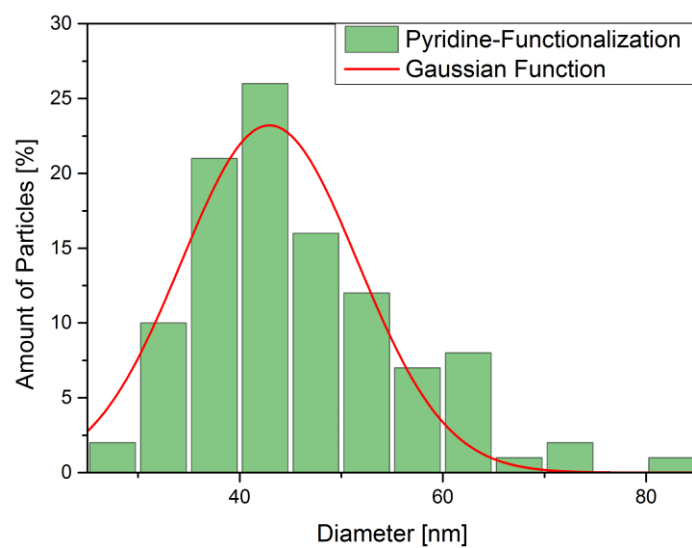


Figure S15: Particle size distribution of pyridine-functionalized MIL-101(Cr) determined from the SEM micrograph in Figure S10.

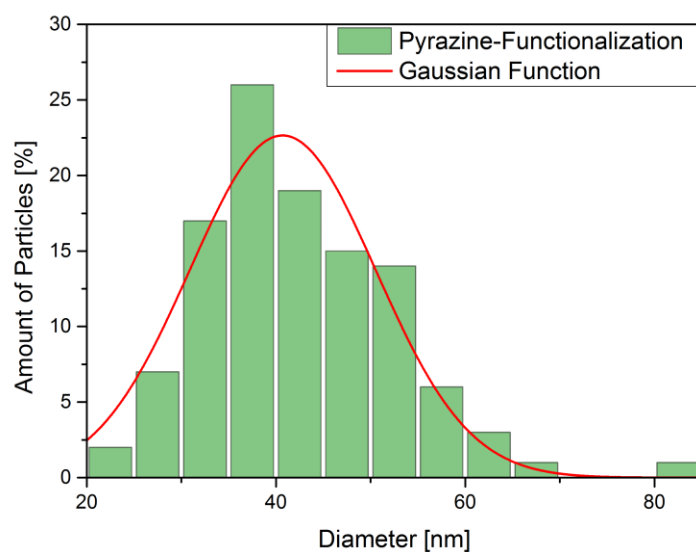


Figure S16: Particle size distribution of pyrazine-functionalized MIL-101(Cr) determined from the SEM micrograph in Figure S12.

Table S3: Results of particle size distribution analysis from the SEM images.

Sample	MIL-101(Cr)	Pyridine-Functionalization	Pyrazine-Functionalization
Particle Diameter [nm]	41	43	41
Standard Deviation [nm]	10	9	10

Dynamic Light Scattering and Zeta-Potential measurements

Figure S17 depicts the pH dependent Zeta-Potential of MIL-101(Cr) nanoparticles in aqueous solution. At pH = 2 starting from around 30 mV, the potential drops for increasing pH. In the initial acidic conditions, the particles are stable and not agglomerated. When reaching pH = 7 upwards, the Zeta-Potential passes through 0 mV, which causes the particles to agglomerate.

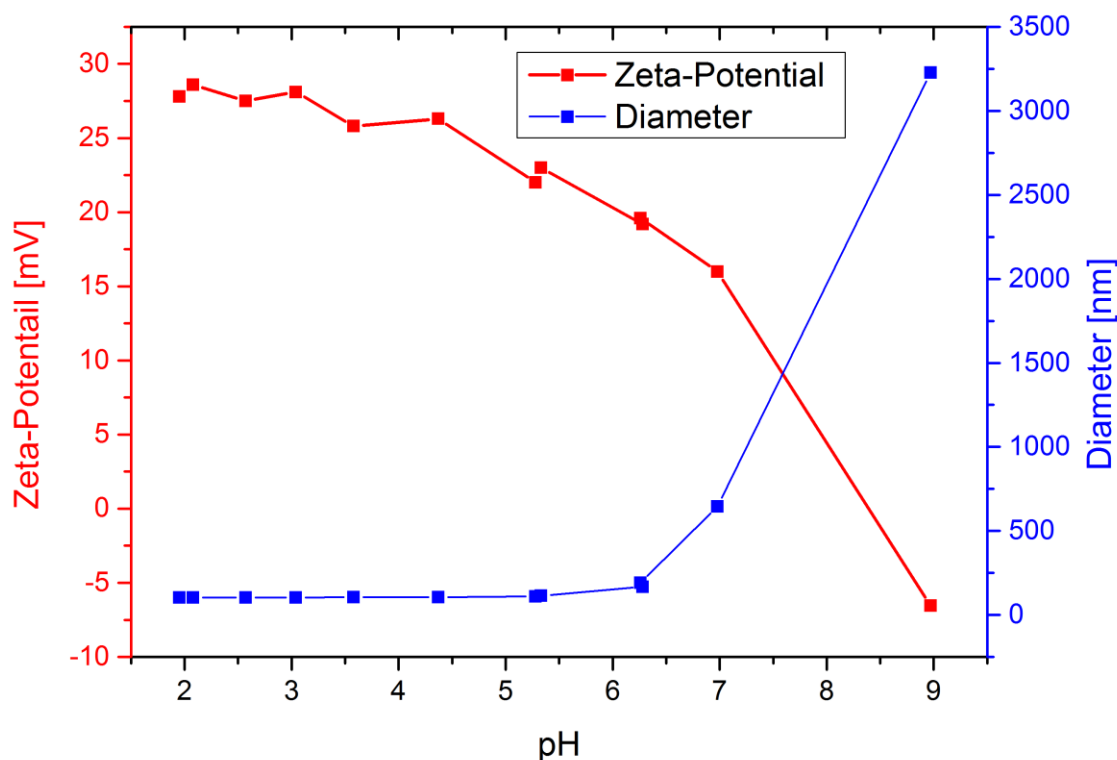


Figure S17: Zeta-Potential of an aqueous solution of MIL-101(Cr) nanoparticles, when titrating from pH = 2 to pH = 7.

The results of the DLS-measurements for the functionalized and unfunctionalized MIL-101(Cr) nanoparticles in ethanol are given in Figure S18. Table S4 gives the average intensity-based diameter of the nanoparticles along with their polydispersity index. Overall, the DLS based hydrodynamic diameter of the particles was not measurably altered by their functionalization. In all three cases, the particles show a similar size around 105 nm and a very monodisperse particle size distribution.

DLS measurements reported in the main text for pyridine-functionalized MIL-101(Cr) nanoparticles in HFE-7100/EtOH and 50 mM Glycine-HCl/Water mixtures were acquired during the density measurements.

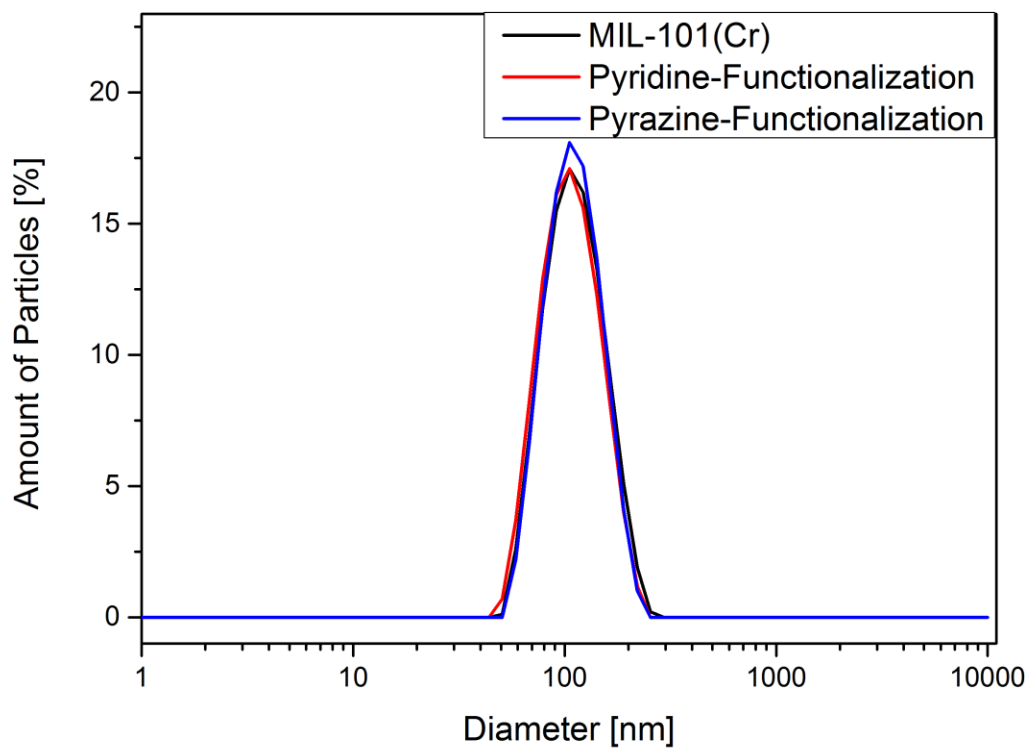


Figure S18: Intensity based particle size distribution of functionalized and non-functionalized MIL-101 (Cr) nanoparticles in ethanol.

Table S4: Summarized results of the DLS measurements for each of the particle species shown in Figure S18.

Sample	Diameter [nm]	Polydispersity Index
MIL-101(Cr)	105	0.088
Pyridine-Functionalized	105	0.174
Pyrazine-Functionalized	106	0.066

Thermogravimetric Analysis

The thermogravimetric analysis for the MIL-101(Cr) nanoparticle sample and its functionalized derivatives is shown in Figure S19. All three samples show similar stability. All samples feature a degradation range between 327 – 374 °C. The values of the residual masses of the nanoparticle species are slightly shifted. This may be due to several causes: Due to the pyridine/pyrazine functionalization, the overall ratio of the solvent/framework masses is altered by the additional mass of the introduced molecules and the varying capability of the nanoparticle species to incorporate solvent molecules. The functionalization approach overall however did not influence the framework stability.

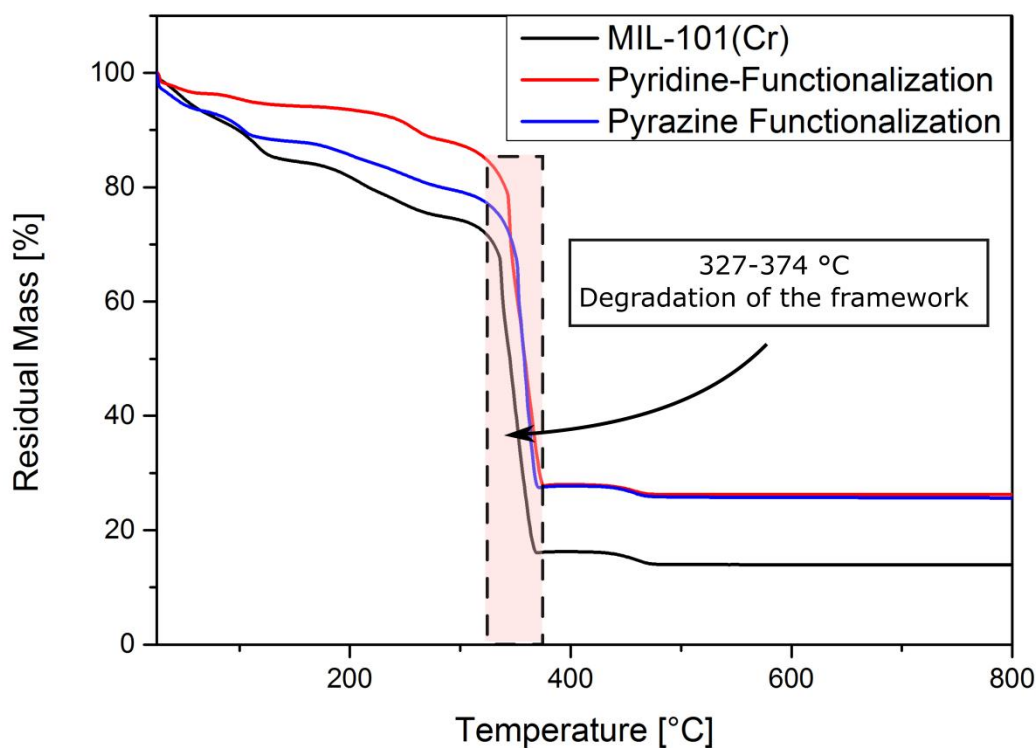


Figure S19: Thermogravimetric analysis of MIL-101(Cr) nanoparticles, pyridine-functionalized MIL-101(Cr) nanoparticles, and pyrazine-functionalized MIL-101(Cr) nanoparticles.

Elemental Analysis

In order to estimate the degree of functionalization of the MIL-101(Cr) species, elemental analysis (CHNS) was performed. The results are summarized in Table S5.

Table S5: Elemental analysis results.

Sample	Mass [mg]	wt% N	wt% C	wt% H
MIL-101(Cr)	4.882	$0.87 \pm 0.3\%$	$18.50 \pm 0.3\%$	$6.85 \pm 0.3\%$
Pyridine-Functionalization	4.905	$2.11 \pm 0.3\%$	$23.69 \pm 0.3\%$	$6.56 \pm 0.3\%$
Pyrazine	4.595	$1.37 \pm 0.3\%$	$20.20 \pm 0.3\%$	$6.67 \pm 0.3\%$

Functionalization				
-------------------	--	--	--	--

This data has been interpreted in the following way: In the pure MIL-101(Cr) MOF sample, a small amount of residual nitrogen is trapped within the framework. This is caused by remnants of the synthesis that are located within the highly porous framework and cannot be removed via exchanging the solvent. This residue was subtracted from the wt% of the pyrazine- and pyridine-functionalized samples. The difference was assumed to be caused by pyridine and pyrazine-functionalization respectively. Based on the crystallographic data from the group of Férey,^[30] the theoretical wt% of nitrogen in pyridine and pyrazine-functionalized MIL-101(Cr) was calculated and compared with the experimental results. This resulted in a functionalization of $(26.8 \pm 9.2)\%$ for the pyridine functionalized sample and $(5.4 \pm 4.6)\%$ for the pyrazine-functionalized sample.

Nitrogen Sorption

The results of the BET calculation of the nitrogen sorption experiments are summarized in Table S6. The corresponding Isotherms are shown in Figure S20. The BET-surface was reduced both for the pyridine and the pyrazine-functionalization. This is expected, since the aromatic groups use up space within the framework. The greater reduction in case of pyrazine is expected as well, since the functionalization degree for pyridine was higher than for the pyrazine-functionalized sample. The pyrazine-functionalization had no notable effect on the pore size distribution of the sample. The pyridine-functionalization did reduce the amount of pores in the 3 nm range, however they are still present. This might be attributed to the greater functionalization degree of the pyridine-functionalized sample. As shown in the XRD experiments, this had no influence on the structure of the MOF.

Table S6: Results of the BET analysis.

Sample	MIL-101(Cr)	Pyridine-Functionalization	Pyrazine-Functionalization
BET-surface area [m ² /g]	4789	3194	3506
Relative pressure range used for calculation	0.11-0.23	0.07 - 0.18	0.07-0.21
Correlation coefficient	0.999	0.999	0.999
C-constant	positive	positive	positive

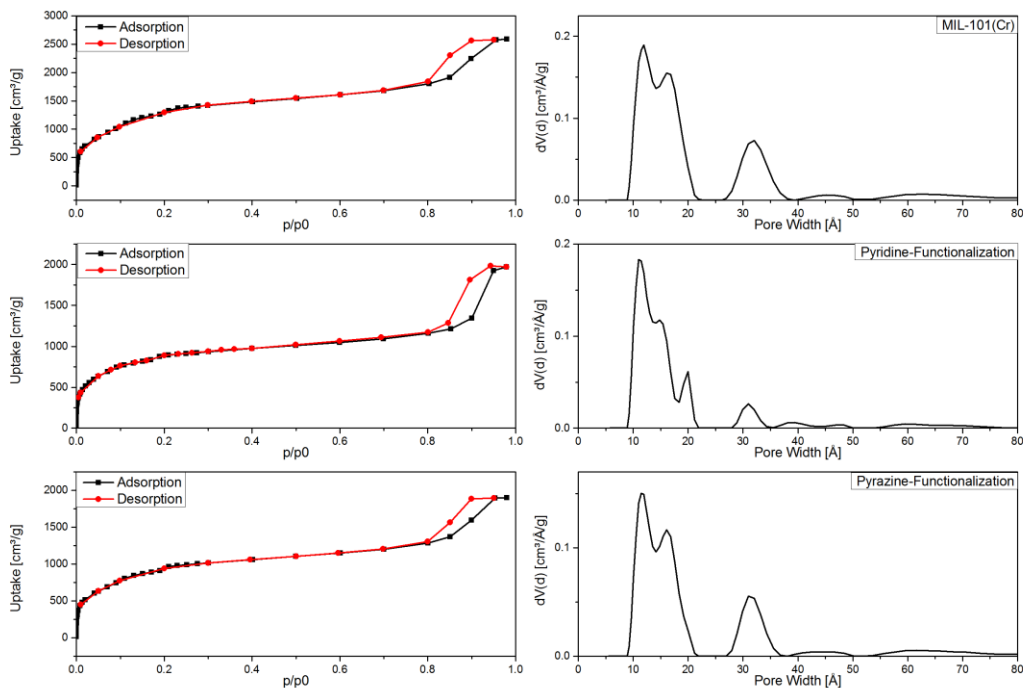


Figure S20: Results of Nitrogen Sorption Experiments of MIL-101(Cr) (top) and the pyridine-(middle) and pyrazine-functionalized (bottom) species.

Porosity Estimation and Calculation of the density of dry MIL-101(Cr)

The density of dry MIL-101(Cr) at $0.66 \frac{\text{g}}{\text{cm}^3}$ was calculated using literature crystallographic data [30] from which all free solvent molecules were removed, and by dividing the mass of the remaining atoms in the elementary cell of the structure by the cell volume. This modified crystal structure was then used for an estimation of the porosity of MIL-101(Cr). The data were evaluated using the “Atom Volumes & Surfaces” tool of the software package Materials Studio v7.0 (Accelrys Software Inc.). The program was used to calculate a probe-molecule dependent Connolly surface with a grid interval of 0.75 Å. The program also provides an occupied and free volume within the elementary cell. This free volume and the total volume of the elementary cell were then used to calculate the porosity of the crystal structure. With the probe radius set to 0 Å the porosity equals 84.5%. The corresponding Connolly surface is shown in Figure S21. Using a probe radius of 1.4 Å to simulate water, the porosity of the framework equaled 82.1%. In case of ethanol, a probe radius of 2.2 Å was assumed resulting in a porosity of 79.1%.

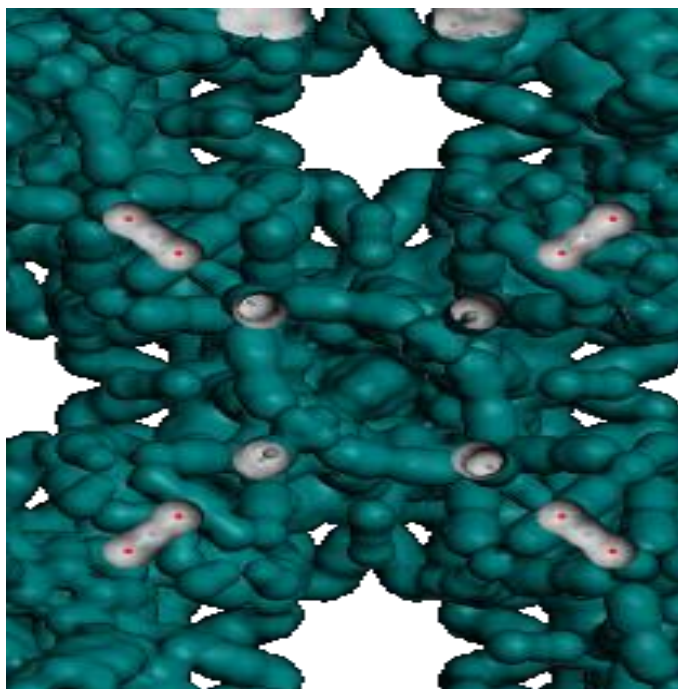


Figure S21: Connolly surface of MIL-101(Cr).

References

- [1] X. Meng, B. Gui, D. Yuan, M. Zeller, C. Wang, *Sci. Adv.* **2016**, 2, e1600480.
- [2] M. Zhao, K. Deng, L. He, Y. Liu, G. Li, H. Zhao, Z. Tang, *J. Am. Chem. Soc.* **2014**, 136, 1738.
- [3] B. Ghalei, K. Sakurai, Y. Kinoshita, K. Wakimoto, A. P. Isfahani, Q. Song, K. Doitomi, S. Furukawa, H. Hirao, H. Kusuda, S. Kitagawa, E. Sivaniah, *Nat. Energy* **2017**, 2, 17086.
- [4] G. Lu, S. Li, Z. Guo, O. K. Farha, B. G. Hauser, X. Qi, Y. Wang, X. Wang, S. Han, X. Liu, J. S. DuChene, H. Zhang, Q. Zhang, X. Chen, J. Ma, S. C. J. Loo, W. D. Wei, Y. Yang, J. T. Hupp, F. Huo, *Nat. Chem.* **2012**, 4, 310.
- [5] S. Wuttke, M. Lismont, A. Escudero, B. Rungtaweeworanit, W. J. Parak, *Biomaterials* **2017**, 123, 172.
- [6] H. Furukawa, U. Müller, O. M. Yaghi, *Angew. Chemie Int. Ed.* **2015**, 54, 3417.
- [7] Z. Li, J. C. Barnes, A. Bosoy, J. F. Stoddart, J. I. Zink, *Chem. Soc. Rev.* **2012**, 41, 2590.
- [8] M. W. Tibbitt, J. E. Dahlman, R. Langer, *J. Am. Chem. Soc.* **2016**, 138, 704.
- [9] C. Walkey, J. Olsen, H. Guo, A. Emili, W. Chan, *J. Am. Chem. Soc.* **2011**, 134, 2139.
- [10] H. Furukawa, N. Ko, Y. B. Go, N. Aratani, S. B. Choi, J. Kim, O. M. Yaghi, *Science* **2010**, 329, 424.
- [11] S. Wuttke, A. Zimpel, T. Bein, S. Braig, K. Stoiber, A. Vollmar, D. Müller, K. Haastert-Talini, J. Schaeske, M. Stiesch, G. Zahn, A. Mohmeyer, P. Behrens, O. Eickelberg, D. A. Bölükbas, S. Meiners, *Adv. Healthc. Mater.* **2017**, 6, 1.

- [12] S. A. MacParland, K. M. Tsoi, B. Ouyang, X. Z. Ma, J. Manuel, A. Fawaz, M. A. Ostrowski, B. A. Alman, A. Zilman, W. C. W. Chan, I. D. McGilvray, *ACS Nano* **2017**, *11*, 2428.
- [13] Y. Sakata, S. Furukawa, M. Kondo, K. Hirai, N. Horike, Y. Takashima, H. Uehara, N. Louvain, M. Meilikhov, T. Tsuruoka, S. Isoda, W. Kosaka, O. Sakata, S. Kitagawa, *Science* **2013**, 339.
- [14] H. Goesmann, C. Feldmann, *Angew. Chemie Int. Ed.* **2010**, *49*, 1362.
- [15] B. Rungtaweeworant, Y. Zhao, K. M. Choi, O. M. Yaghi, *Nano Res.* **2016**, *9*, 47.
- [16] S. Xu, Z. Nie, M. Seo, P. Lewis, E. Kumacheva, H. A. Stone, P. Garstecki, D. B. Weibel, I. Gitlin, G. M. Whitesides, *Angew. Chemie Int. Ed.* **2005**, *44*, 724.
- [17] J. Ma, A. P. Kalenak, A. G. Wong-Foy, A. J. Matzger, *Angew. Chemie - Int. Ed.* **2017**, *56*, 14618.
- [18] P. Hirschle, T. Preiß, F. Auras, A. Pick, J. Völkner, D. Valdepérez, G. Witte, W. J. Parak, J. O. Rädler, S. Wuttke, *CrystEngComm* **2016**, *18*, 4359.
- [19] C. Y. Tay, M. I. Setyawati, J. Xie, W. J. Parak, D. T. Leong, *Adv. Funct. Mater.* **2014**, *24*, 5936.
- [20] J. Park, H. Elmlund, P. Ercius, J. M. Yuk, D. T. Limmer, Q. Chen, K. Kim, S. H. Han, D. A. Weitz, A. Zettl, A. P. Alivisatos, *Science* **2015**, 349.
- [21] M. Sin, C. Kutzscher, I. Senkovska, T. Ben, S. Qiu, S. Kaskel, E. Brunner, *Microporous Mesoporous Mater.* **2017**, *251*, 129.
- [22] M. M. Modena, Y. Wang, D. Riedel, T. P. Burg, *Lab Chip* **2014**, *14*, 342.
- [23] G. Férey, C. Mellot-Draznieks, C. Serre, F. Millange, J. Dutour, S. Surblé, I. Margiolaki, *Science* **2005**, 309.
- [24] S. Wuttke, C. Dietl, F. M. Hinterholzinger, H. Hintz, H. Langhals, T. Bein, *Chem. Commun.* **2014**, *50*, 3599.
- [25] P. H. Brown, A. Balbo, H. Zhao, C. Ebel, P. Schuck, *PLoS One* **2011**, *6*, DOI 10.1371/journal.pone.0026221.
- [26] H. Eisenberg, *Biophys. Chem.* **2000**, *88*, 1.
- [27] S. Wuttke, S. Braig, T. Preiß, A. Zimpel, J. Sicklinger, C. Bellomo, J. O. Rädler, A. M. Vollmar, T. Bein, *Chem. Commun.* **2015**, *51*, 15752.
- [28] "Useful Latex Bead Formulae," can be found under www.thermofisher.com/ch/en/home/life-science/cell-analysis/qdots-microspheres-nanospheres/idc-surfactant-free-latex-beads/latex-bead-technical-overview/useful-latex-bead-formulae.html#latex, **n.d.**
- [29] † O. I. Lebedev, *,‡ F. Millange, ‡ C. Serre, † and G. Van Tendeloo, § G. Férey‡, **2005**, DOI 10.1021/CM051870O.
- [30] G. Férey, C. Mellot-Draznieks, C. Serre, F. Millange, J. Dutour, S. Surblé, I. Margiolaki, **2006**, DOI 10.5517/CCNB2LM.